Optical Coherence Elastography of Engineered and Developing Tissue

**HAN-JO KO, B.S.,[1] WEI TAN, Ph.D.,[2,5] RON STACK, M.S.,[2]
and STEPHEN A. BOPPART, M.D., Ph.D.[1–4]**

ABSTRACT

Biomechanical elastic properties are among the many variables used to characterize *in vivo* and *in vitro* tissues. Since these properties depend largely on the micro- and macroscopic structural organization of tissue, it is crucial to understand the mechanical properties and the alterations that occur when tissues respond to external forces or to disease processes. Using a novel technique called optical coherence elastography (OCE), we mapped the spatially distributed mechanical displacements and strains in a representative model of a developing, engineered tissue as cells began to proliferate and attach within a three-dimensional collagen matrix. OCE was also performed in the complex developing tissue of the *Xenopus laevis* (African frog) tadpole. Displacements were quantified by a cross-correlation algorithm on pre- and postcompression images, which were acquired using optical coherence tomography (OCT). The images of the engineered tissue were acquired over a 10-day development period to observe the relative strain differences in various regions. OCE was able to differentiate changes in strain over time, which corresponded with cell proliferation and matrix deposition as confirmed with histological observations. By anatomically mapping the regional variation of stiffness with micron resolution, it may be possible to provide new insight into the complex process by which engineered and natural tissues develop complex structures.

INTRODUCTION

NATURAL BIOLOGICAL TISSUES are classified as inhomogeneous, viscoelastic, nonlinear, and anisotropic, because of their complex structure and composition. However, it still remains to be determined what aspects of these biomechanical properties are essential for engineering a robust tissue replacement. Numerous studies have shown the importance of mechanical stimulation during the development.[1–4] Intracellular cytoskeleton networks and extracellular matrix, including fibulins, cadhesins, microtubules, fibronectin microfibrils, and proteoglycan aggregates (to name a few), can serve as intrinsic regulators and adaptors to modulate intercellular communication and differentiation. Previous studies have also demonstrated that mechanical forces modify metabolic performance and gene expression in certain tissues.[5,6] In addition, pathological disease processes are responsible for either increasing or decreasing the elastic tissue properties. Our understanding of cell mechanics and cell biology has established significant data to compare cell mechanics between normal and diseased states.[7] By utilizing quasistatic magnetic resonance elastography (MRE), quantitative information concerning tissue elas-

---

[1]Department of Electrical and Computer Engineering, [2]Beckman Institute for Advanced Science and Technology, [3]Department of Bioengineering, [4]College of Medicine, University of Illinois at Urbana—Champaign, Urbana, Illinois.

[5]Currently, Departments of Mechanical Engineering and Pediatric Cardiology, University of Colorado, Health Sciences Center, Boulder, Colorado.

ticity has been acquired both in ablated tissue and breast cancer tissue.[8,9] In ultrasound imaging, transient elastography has made possible not only the *in vivo* measurement of biomechanical properties in soft tissues, but also the detection of breast tumors.[10,11]

Needless to say, a close relationship between mechanical stimulus and physiological function is evident. By combining elastography with various imaging modalities such as ultrasound, magnetic resonance imaging, and optical coherence tomography, in particular, it is possible to extract not only anatomical structural features but also biomechanical tissue properties. While several investigators have focused on small animal tumor models to show the feasibility of elastography to quantify elastic moduli,[10,12,13] few studies have investigated the application of elastography to developing engineered tissues or biological organisms at embryonic and early stages of growth.

The elastic properties depend greatly on the molecular composition of tissue, as well as the micro- and macroscopic structural organization. Young's modulus, Poisson's ratio, and viscosity, for instance, can be quantified by elastic imaging and be mapped in an anatomically meaningful presentation. By idealizing tissue as an elastic material, 81 stiffness constants are needed to specify the elastic behavior.[14] With the common assumption that the tissue is orthotropic and homogeneous, only two constants, Young's modulus and Poisson's ratio are required to describe the response to mechanical loads. With quasistatic compression in homogeneous tissue, Poisson's effect is negligible and remains constant. Elastography focuses on the estimation of the strain tensors after a quasistatic compression is applied because only strain distribution may be directly estimated in practice.[15] From strain distribution, shear modulus is available, and the nonlinearity of the relationship between shear moduli and Young's moduli is simplified by additional assumptions, such as the approximation of tissue as an isotropic material. As a result, elastic properties can be quantified.[16] To better characterize these biomechanical properties, models specifically addressing the shear elastic moduli and the relationship between shear moduli and Young's moduli have been proposed to explain the biomechanical properties of physiological phenomena.[17–19]

While cellular imaging resolutions are highly desired to obtain biomechanical properties in biological samples quantitatively, achieving these resolutions often requires biopsy and histopathologic examination, which unfortunately alters the biomechanical properties and the viability of the tissues. A variety of imaging modalities have been utilized to noninvasively visualize biological tissues at macroscopic morphologic levels, including magnetic resonance imaging and ultrasound. Since these modalities differ in cost and capabilities, such as resolution, depth of penetration, and contrast selectivity, a comparison is provided in Table 1. Intrinsic limitations exist, however, for each imaging modality. Advantages of ultrasound elastography include cost-effectiveness and portability while magnetic resonance elastography enables whole-body imaging in humans and the ability to estimate anisotropic and viscous properties in heterogeneous samples.[20,21] In magnetic resonance elastography, quantitative values of the shear modulus are estimated by the local wavelength of the compressive wave. Since strain waves attenuate rapidly at high frequencies, longer wavelengths are needed to penetrate deeper while maintaining high spatial resolution in noisy images, which creates uncertainties in approximating local wavelengths.[22] In ultrasound elastography, typical imaging resolution is between 125 and 200 μm.[23] It has been shown that the axial resolution in ultrasound elastography is mainly limited by the bandwidth and the central frequency of the transducer in the ultrasound system.[24]

Optical coherence tomography (OCT) is an emerging high-resolution biomechanical imaging technology that has overcome many of the limitations of noninvasive cellular level imaging in highly scattering (nontransparent) tissues.[25,26] By utilizing low-coherence interferometry,[27,28] OCT performs optical ranging within a sample to gather information about the time-of-flight delay from reflective boundaries and backscattering regions.[29,30] A large number of studies have demonstrated the potential for using OCT to investigate and facilitate the diagnosis of disease, direct therapeutic intervention, and imaging *in vivo* arterial pathology in humans, as well as many other applications in gastroenterology, urology, and neurosurgery.[31–35] OCT has also been used to demonstrate the microstructural changes that occur during the com-

TABLE 1.   COMPARISON OF DIFFERENT IMAGING AND ELASTOGRAPHY MODALITIES

	Resolution	Imaging depth	Field of view	Costs	Acquisition rate
Clinical US	100–200 μm	30 cm	20 cm	$50–100K	Video rate
Research US	2 μm	50 μm	mm-cm	$30–50K	Video rate
Clinical MRI	0.1–1.0 mm	Full body	Full body	> $2 mil.	50 ms
Research MRI	5 μm	1 cm	1 cm	> $1 mil.	12 hrs
OCT	1–10 μm	3 mm	mm-cm	$30–50K	Video rate

plex process of development in several developmental biology specimens.[36–39] Compared to other imaging modalities, OCT permits high-resolution real-time imaging over extended periods of time. OCT is capable of identifying microstructures in the biological tissues based on their optical backscattering properties (optical index of refraction), with image resolutions approaching that of conventional histology. Imaging based on optical backscattered light is possible since, in general, most biological tissue have a sufficient number of scattering objects (membranes, organelles, nuclei, etc.) to produce contrast in OCT images. Nevertheless, a comparatively small number of studies have been devoted to investigating *in vitro* engineered tissues.[40,41]

In this paper, we combine the high-resolution real-time imaging capabilities of OCT with elastography techniques to perform optical coherence elastography (OCE). In the past, elastic studies in tissues of the cardiovascular system using OCE have measured reduced elasticity of extracardiac arteries and veins, which has been associated with coronary disease.[42–45] Here, the use of OCE permits the investigation of the biomechanical properties in engineered tissues, as well as in developing natural biological specimens at different stages. By mapping both the structural anatomical components of developing engineered and natural tissues with regional biomechanical tissue properties, OCE has significant potential for quantitatively determining the evolving biomechanical properties and demonstrating how these properties not only affect the microstructural organization of tissue, but also contribute to the biocompatibility of engineered tissues.

MATERIALS AND METHODS

This study investigates the evolving regional differences of biomechanical strain in engineered tissues and maps the strain distributions in a complex yet commonly used developmental biology animal model, the African frog tadpole (*Xenopus laevis*).

Engineered tissue preparation

Our engineered tissue model consisted of NIH-3T3 cells (ATCC) seeded in a three-dimensional collagen matrix. A mixture of 1.2 mg/mL collagen (250 μL), 0.1M NaOH (25 μL), 5% NaHCO$_3$ (10 μL), 10 $\times$ HBSS (60 μL), and PBS (culturing media) was first prepared on ice. Acetic acid was used to adjust pH to 7.4–7.6, and 6 μm diameter polystyrene microspheres (3.6 $\times$ 10^4 microspheres/mL, Polyscience, Niles, IL) were added before mixing with the cells. The microspheres were added to provide optical scattering centers that were detectable using OCE. At early stages of engineered tissue development, the low backscattering properties of individual cells

did not permit them to be resolved by OCE since low-density populations of cells in a low-scattering matrix are not as highly scattering as most natural biological tissues. Cell concentration (1.25 $\times$ 10^5 cells/mL) was kept constant throughout all samples. Samples containing only cells and collagen matrix and samples containing only microspheres and collagen matrix served as external controls.

The imaged samples were composed of two adjacent regions. One half was prepared using the method described previously, while a second adjacent region contained all of the same constituents except for cells, thereby providing a standardized internal control within each of the acquired images. The mixtures were then incubated in a 37°C, 5% CO$_2$ incubator for 20 min to solidify the collagen gel. Culturing medium was then added to prevent dehydration and was replaced with fresh solution every 3 days. OCE data were taken on days 0, 3, 7, and 10.

Animal model

Xenopus laevis (African frog) tadpole specimens (24–48 h after fertilization) were purchased commercially (Connecticut Valley Biological Supply, Southampton, MA) and kept in a solution of 1/10 $\times$ modified Barth's saline at room temperature with a 12 h dark cycle. Specimens were maintained in aquarium tanks and fed a standard prepared diet (*Xenopus* powder/pellets, Connecticut Valley Biological Supply) daily. These animals were cared for and maintained under the established and approved protocols of the University of Illinois Institutional Animal Care and Use Committee. Images were acquired after tadpoles were anesthetized by immersing in 0.05% benzocaine until they no longer responded to tactile stimuli. Tadpoles were oriented on the imaging stage such that the light beam from the OCT system sample arm was incident on the dorsal side and the scan line was aligned perpendicular to the long axis of the specimen.

Optical coherence elastography

A Nd:YVO$_4$-pumped titanium:sapphire laser was used as a broad-bandwidth optical source in the OCE system. The output was at a center wavelength of 800 nm, an average power of 500 mW, and composed of 90 fs pulses at an 80 MHz repetition rate. The output from the laser was coupled into an ultrahigh-numerical-aperture fiber (UHNA4, Thorlabs, Newton, NJ) to spectrally broaden the light from 20 to >100 nm and improve the axial resolution,[46] which was measured to be 6 μm. The reference arm of the OCT interferometer contained a galvanometer-driven retroreflector delay line that was scanned a distance of 2 mm at a rate of 30 Hz. The sample arm beam was then focused to a measured 10 μm spot size diameter (transverse resolution) using a 20 mm focal length achromatic lens (Fig. 1a). This provided a

(a)

(b)
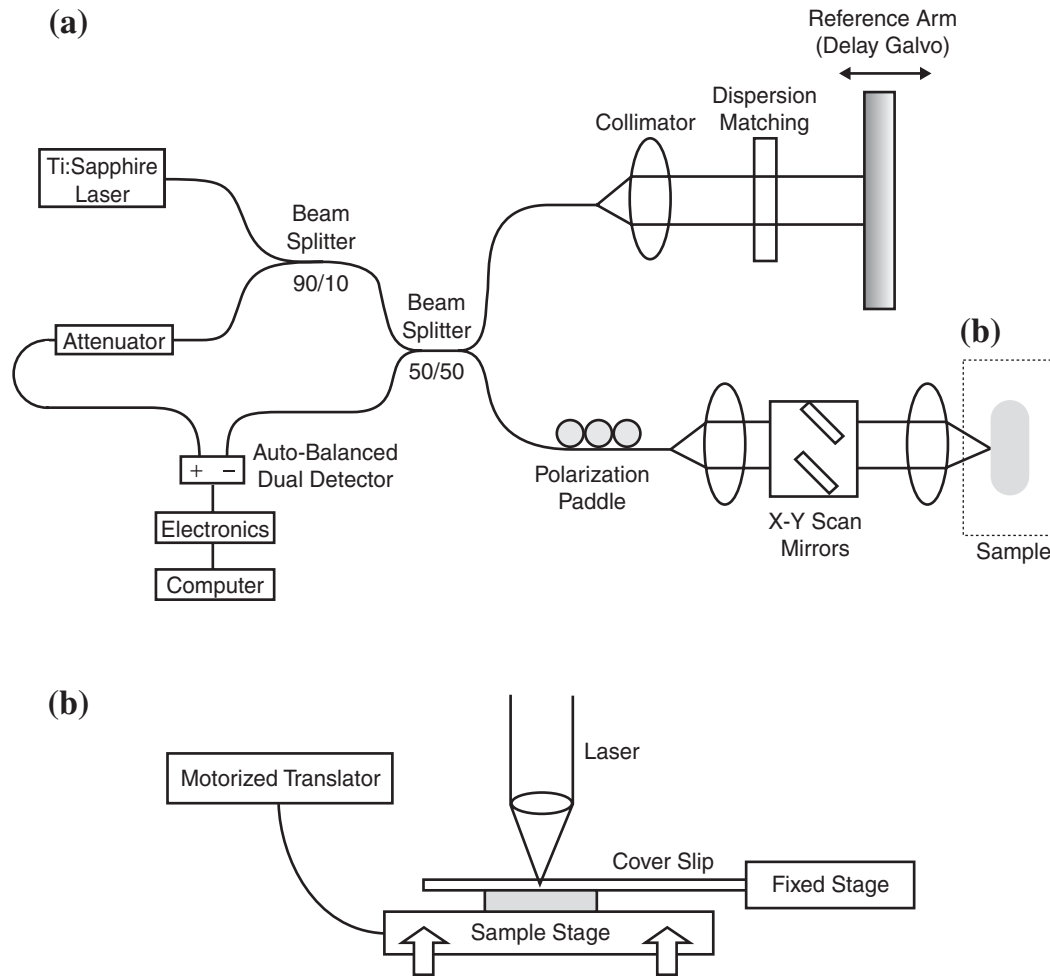
FIG. 1.   OCT/OCE system schematics. (**a**) OCT system schematic. A Nd:YVO$_4$-pumped titanium:sapphire laser is used as an optical source. Light leaving the source is first split 10/90 and then 50/50 by fiber couplers. One of the fibers delivers half of the light to the reference arm containing a linearly translating mirror, and the other directs the remaining half of the light to the sample arm of the interferometer. Additional polarization paddles and dispersion matching glass in the sample arm and the reference arm, respectively, help maximize the interference signal. Dual-balanced detection is implemented to decrease background noise. (**b**) OCE stage schematic. The sample was confined between a fixed upper stage and a sample stage. At least 20 increasing step-like static compressions were introduced by a computer-controlled translation stage. Each compression step was approximately 2 μm for engineered tissues and 8 μm for *Xenopus laevis*.

confocal parameter (depth-of-field) of 196 μm. Reflections from the sample were combined with reflections from the reference arm mirror. Interference fringes were detected by photodiodes only when the reflections from the sample and the reference arm were matched in group delay (coherence length of the light source). By recording the amplitude of the interference signals, as well as the position of the reference mirror, spatial distributions of amplitudes and delays due to sample reflections were acquired. To generate two-dimensional images (2 $\times$ 2 mm, 1024 $\times$ 1024 pixels), the incident beam was mechanically scanned in the transverse direction while multiple axial measurements were acquired. After detection, electronic signals were bandpass filtered to eliminate

noise from outside the signal bandwidth, demodulated at the Doppler-shifted frequency of the moving reference arm, and finally transformed into digital data to display on the computer monitor. The free-space z-axis distance in our images was 2 mm. The image tissues had a measured average refractive index of 1.39. Therefore, the displayed OCT images were scaled in the vertical direction by dividing the free-space distance by the average index to reflect the optical z-axis distance of approximately 1.44 mm. The gray-scale OCT images represent the spatial distribution of the backscattered optical intensity within the tissue.

A glass cover slip was used as a fixed and transparent upper boundary while a computer-controlled translation

stage moved the samples upward and applied the necessary static compressions to the samples against the fixed glass cover slip (Fig.1b). Each compression step was approximately 2 μm for engineered tissues and 8 μm for *Xenopus laevis* tadpoles. OCT images were acquired after each static compression, forming sets of 20 to 30 images and sequences representing the changing scattering positions following each static compression.

One technique for measuring the displacement (x_d, z_d) on a two-dimensional image is to compute the normalized cross-correlation (ρ) of specific pixels within a predefined window (X, Z) using the following formula in a discrete form.[42]

$$\rho(x',z') =$$

$$\frac{\int_{-Z/2}^{Z/2}\int_{-X/2}^{X/2} I_1(x,z)I_2(x-x',z-z')dxdz}{\sqrt{\int_{-Z/2}^{Z/2}\int_{-X/2}^{X2} I_1{}^2(x,z)dxdz \int_{-Z/2}^{Z/2}\int_{-X/2}^{X/2} I_2{}^2(x-x',z-z')dxdz}}$$

I_1 and I_2 are functions of (x, z) where x is the transverse location and z is the axial (depth) location in the two-dimensional cross-sectional images. The position of the pixels that give the maximum of the resultant cross-correlation function within the kernel size is the estimated displacement (x_d, z_d), when the normalized cross-correlation (ρ) is usually close to one. Given known displacements of (x_d, z_d), these displacements were optimally detected using a kernel of size $(2x_d, 2z_d)$, which was determined empirically during these studies. In order to remove undesired background noise from the images, a user-adjustable threshold was programmed into the algorithm to neglect low-signal pixels associated with image noise.

After regional displacements were obtained within each pair of images in a compression sequence, displacement maps were generated and color-coded to allow for the visual representation of regional changes. Figure 2s shows the full spectrum of the color map for displacements. The color corresponds to the direction (θ) of the displacement, while the intensity of the color represents the distance of estimated displacement (γ). The radius of the color map circle was defined by the average of the displacements $\times$ 1.5 to fully utilize the color gradient available.

The strains (ε) were determined pixel by pixel by using the formula $\varepsilon = \dfrac{\Delta L}{}$ in a continuous form, where ΔL represents the displacement of a specific pixel and L represents the distance from the bottom of the engineered tissue to the pixel position. Related strain maps corresponding to the anatomical scattering data were generated by taking the derivative of the displacements with respect to the position in the axial direction. Figure 2t shows the full spectrum of the color map for strains where red represents the maximum value and violet represents the minimum value in the image. Color scales were normalized for each set of structural, displacement, and strain images.

Statistical analysis

To better quantify the changes within the engineered tissues, average strains in both the cell-seeded and cell-free regions were calculated for days 0, 3, 7, and 10 after each of the first three compressions. The lower (deepest) boundary of each region was chosen as the limit at which the pixel intensity dropped to 5% of the maximum. Pixels with lower intensities were considered noise and were excluded from the average strain calculations. In addition, the selected cell-seeded and cell-free regions were at least 400 μm away from the interfacial boundary to exclude any effects from the interaction between these two sample types. The cell-free regions, which contained only matrix components, served as internal image references over the 10 days of the experiment, and a ratio of average strain in the cell-seeded regions to that in the cell-free regions was calculated after each of the three compressions throughout the duration of the study.

Histological processing

Following imaging, all samples were fixed in 3.7% formaldehyde for at least 24 hours, embedded in paraffin, cut into 40 μm-thick sections with a microtome, and stained with hematoxylin and eosin for light microscopy observations. Nuclei were stained blue by hematoxylin while connective tissues and extracellular matrix were stained magenta by eosin. A section thickness of 40 μm was chosen to increase the number of cells available in each section since these and other engineered tissues have relatively lower cell densities than natural biological specimens. Sections were analyzed and quantified (Photoshop 7.0, Adobe Systems, San Jose, CA) for eosin (magenta) color changes, which were attributed to increases in secreted extracellular matrix by cells in the engineered tissues at later stages. The percentage of magenta in the background was recorded via histogram data, which was divided into 256 levels with values of 0 and 255 corresponding to the most and least color saturation, respectively.

RESULTS

Engineered tissue

Figure 2a–d show representative structural OCT images of the engineered tissues on days 0, 3, 7, and 10, respectively. Darker highly scattering point-like objects are the embedded microspheres, while collagen and cells re-
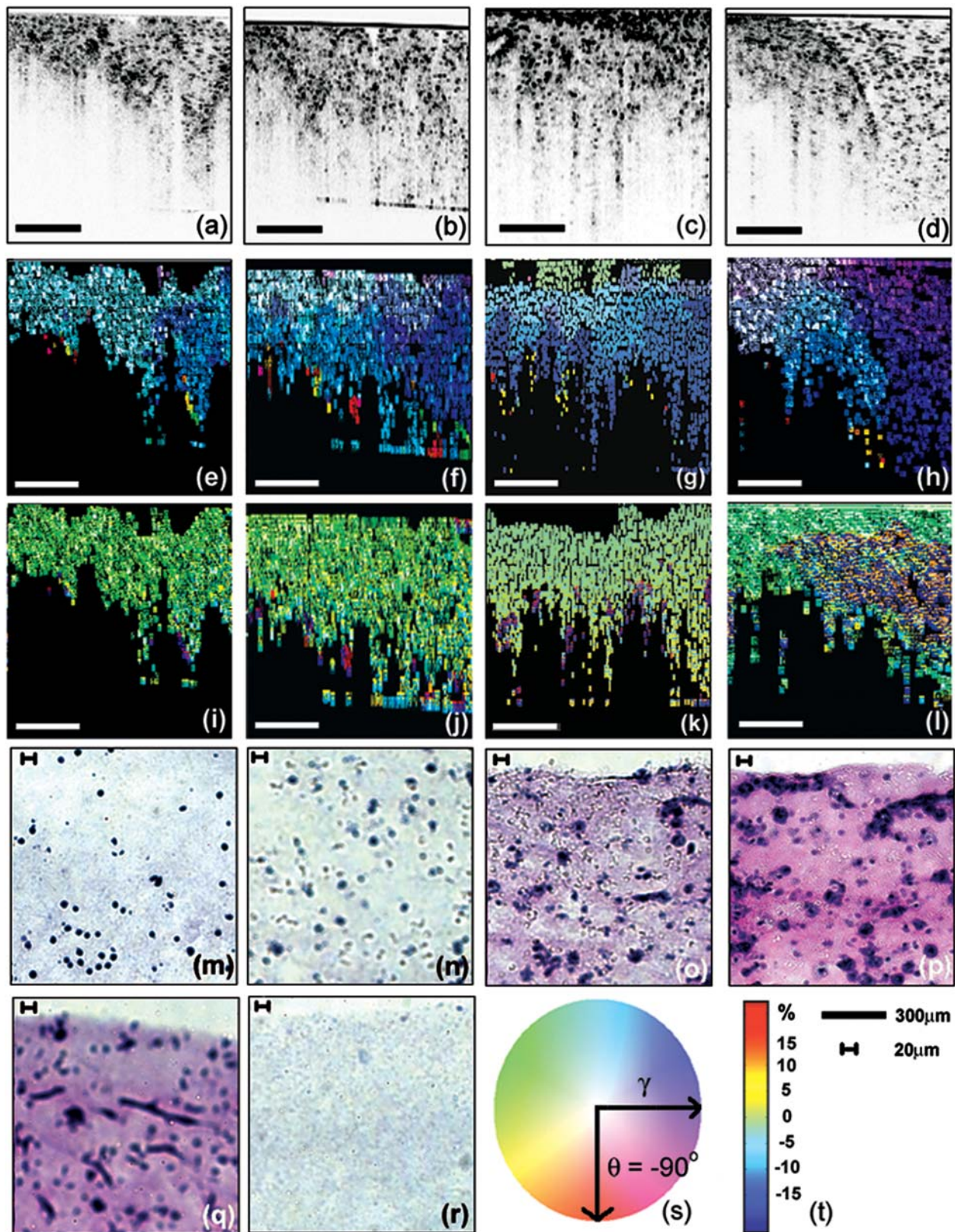
FIG. 2. Images of engineered tissues. (**a–d**) Structural OCT images on days 0, 3, 7, and 10, respectively, of the boundary between the cell-seeded region (left) and the cell-free region (right). (**e–h**) Displacement maps on days 0, 3, 7, and 10, respectively, color-coded using the scale in **s**. (**i–l**) Strain maps on days 0, 3, 7, and 10, respectively, using the color scale in **t**. (**m–p**) Corresponding histology from the cell-seeded tissue regions. (**q**) Histological image of cells after 10 days of incubation without embedded microspheres. (**r**) Histological image of a cell-free scaffold and microspheres. Scale bar, 300 μm in **a–l**; 20 μm in **m–r**. (Images available in color in online version.)
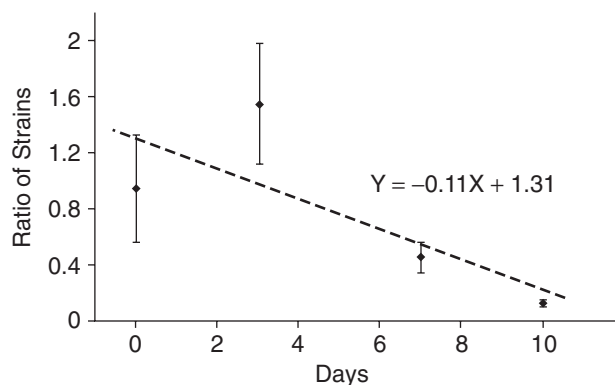
FIG. 3. Relationship between incubation time and ratio of strains in the engineered tissues. Error bars represent standard deviation. A fitted line illustrates the general trend of increasing stiffness (decreased strain) over time.

main poorly scattering at the early stages of culture. The boundary between the cell-seeded and cell-free regions lies approximately in the middle of each image, with the cell-seeded region on the left and the cell-free region on the right. Figure 2e–h shows the color-coded displacement maps, using Figure 2s as the color map with γ equal to 1.5 times the average displacement. Figure 2i–l show corresponding strain maps with corresponding color scale, ranging from +20% to −20%, as shown in Figure 2t.

In the structural OCT image sequence (Fig. 2a–d), no obvious scattering differences are observed over the duration of this study. However, the boundary between the cell-seeded and cell-free regions is more evident toward the end of the duration, when the level of imaging penetration decreases in the cell-seeded region due to more attenuation from the increased number of cells.

The displacement and strain maps have noticeable changes over time. In Figure 2e, the difference in the intensity of color between the two regions is negligible compared with that in Figure 2h, where there is a larger displacement in the cell-free region, indicating that this region is less stiff than the cell-seeded region. The cell-seeded regions of the samples, with increasing cell density, is expected to become stiffer over time, while the cell-free region of the sample is expected to be less stiff and remain relatively constant over the duration of the experiment. This trend can be observed since the cell-free region has been more displaced given the same amount of compression. Also, since the static compression was applied from the bottom of the sample and directed upward, most of the color-coded data appear to be in the range from green to violet, or the combination of the two, which is verified in the displacement maps (Fig. 2e–h).

When these two regions of different biomechanical properties undergo the same amount of mechanical compression, the stiffer (cell-seeded) region tends to exhibit not only vertical displacement, but also slight horizontal displacement into the less stiff cell-free region. Since the

applied compression was only in the axial direction, only the vertical displacements were used to calculate strain in this study, and the data regions used in these calculations were sufficiently far from the interfacial boundary to minimize the nonvertical displacements.

In the strain maps for days 0 and 3 (Fig. 2i–j), one can observe mostly green regions in both the cell-seeded and cell-free regions, suggesting that the two regions share similar biomechanical properties. However, beginning on day 7 (Fig. 2k), observable differences in the biomechanical properties between the two regions begin to appear and are most obvious on day 10, suggesting that the cell-seeded engineered tissue becomes stiffer. This trend is also verified in the corresponding histological images.

Figure 2m–p represent the corresponding histological images of cell-seeded regions on days 0, 3, 7, and 10, respectively. Cells are stained and appear darker than their surroundings, primarily due to hematoxylin. As the incubation time increases, cell density increases. Cells also secrete their own extracellular collagen matrix, which explains the increase in the intensity of the magenta background from eosin. This is in contrast to the background with only microspheres and collagen, which was semi-transparent (Fig. 2r). The increase in the intensity of the magenta background is more apparent after day 7, which corresponds to the changes observed in the strain maps (Fig. 2k). The percentage of eosin (magenta) color in the background increases from 0.39% on day 0 and 0.38% on day 3 to 3.04% on day 7 and 12.64% on day 10.

After normalizing the average strain in the cell-seeded region with that from the cell-free region, the ratio of strains decreases as the incubation time increases (Fig. 3), as summarized in Table 2. This indirect relationship between the incubation time and the displacement/strain is observed with the exception between days 0 and 3. The increase in the ratio of average strains observed on day 3 relative to day 0 may be explained by the fact that, after experiencing environmental shock from the mixing and culturing process, a period of recovery is needed for cells before proliferation. The decrease in standard deviation starting on day 7 is also noted, which further implies that the tissues becomes more uniform as incubation time increases.

A line fitted to the data (Fig. 3) illustrates the general

TABLE 2. STATISTICAL DATA OF ENGINEERED TISSUES ON DAY 0, 3, 7, AND 10

	Mean of ratio of strains (%)	p-values	Percentage of magenta in the background (%)
Day 0	95.1 ± 38.2	—	0.39
Day 3	155.2 ± 43.1	p = 0.1449	0.38
Day 7	39.3 ± 17.5	p = 0.0131	3.04
Day 10	13.7 ± 2.5	p = 0.0069	12.64

trend between incubation time and the ratios of strains. The negative slope indicates that as the incubation time increases, cells are proliferating and attaching to one another as well as to the extracellular matrix, which subsequently increases the stiffness of the engineered tissue. A linear least-squares fit also indicates that there is only a 3% standard error in the resulting slope. Nevertheless, this linear relationship might not completely capture the actual change in strain as a function of time since the cell population is likely to proliferate in a nonlinear fashion prior to reaching a steady-state condition with the maximum number of sustainable cells. Still, a decrease in strain is evident as the incubation time increases.

On day 10, it was observed that cells aggregate in a more organized fashion regardless of whether or not microspheres are embedded (Fig. 2p and q). The degree to which the microspheres are interfering or inhibiting cell growth is, as a result, minimal. Based on these observations, and the presence of microspheres in both the cell-seeded and cell-free regions, it can be inferred that these microspheres are not the major contributor toward changes in the stiffness of the engineered tissue.

Although the resolution of OCT was measured to be 10 μm and 6 μm in the transverse and axial directions,

respectively, it is still possible to observe a 6μm diameter microsphere due to large differences in the refractive indices between the microspheres and the surrounding medium. The lack of highly scattering structure during early development of the engineered tissues necessitates the addition of microspheres to minimize errors when estimating displacements. Microspheres of 6 μm in diameter were chosen so that the shadowing artifacts below the scattering microspheres are reduced to a negligible level. The small diameter also minimizes the optical attenuation and increases OCT imaging penetration.

Animal model

The *Xenopus laevis* (African frog) has been a widely used and well-characterized developmental biology animal model. Despite extensive research in developmental processes, few studies have investigated the *in situ* and evolving biomechanical properties in developing specimens primarily because of the lack of suitable high-resolution nondestructive methods. OCE can address many of these limitations and is used to illustrate variations in strain within a developing tadpole.

Figure 4a and 4b show representative OCT images of
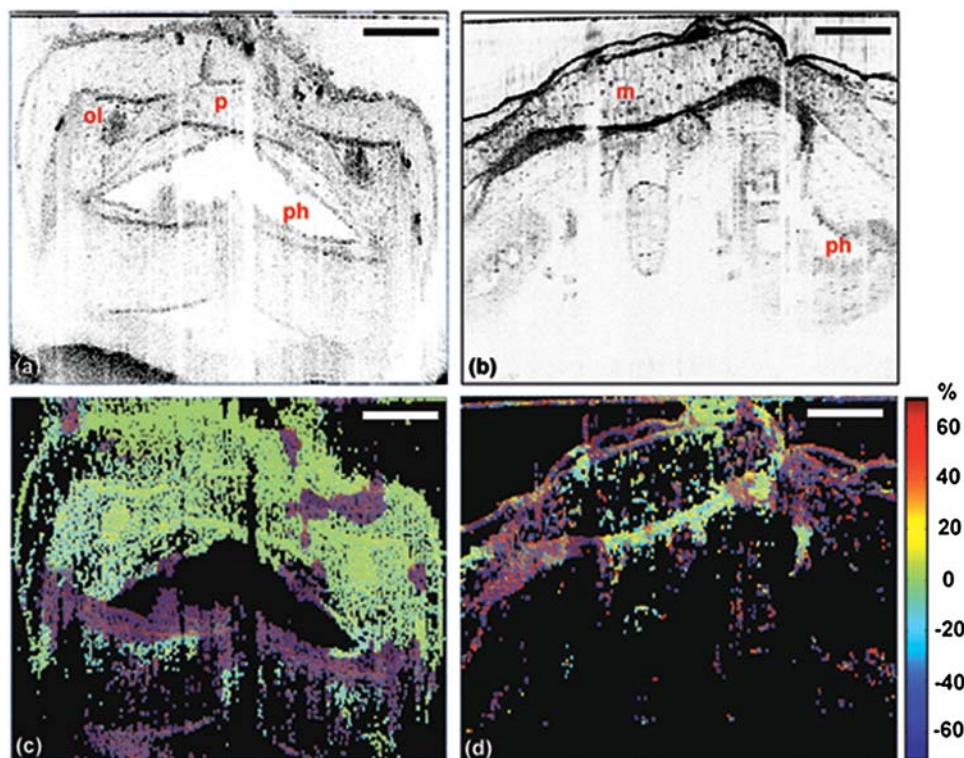
FIG. 4. OCT images and strain maps of a *Xenopus laevis* tadpole at different stages. (**a and c**) Representative structural OCT and OCE strain maps for stage 42 (3 day-old). (**b and d**) Representative structural OCT and OCE strain maps for stage 50 (15 day-old). Compression sequences are available online at ⟨http://biophotonics.uiuc.edu/movies/oce⟩. Abbreviations: m, mesenchymal cells; ol, olfactory nerve; p, parachordal cartilage; ph, pharynx; scale bar, 300 μm. (Images available in color in online version.)

a *Xenopus* tadpole at stages 42 (3-day-old) and 50 (15-day-old), respectively. Figure 4c and 4d are corresponding strain maps with the color scale ranging from $+60\%$ to -40%. Although the displacements from the tadpoles after compression are more random due to the inhomogeneity within the specimen, regional differences are still evident and physiological structures corresponding to these biomechanical differences can be identified in the structural OCT images. There is also more variability in the strain within a *Xenopus* tadpole, both structurally and biomechanically, than in the engineered tissues.

DISCUSSION

Using OCE, this research has demonstrated that the spatially distributed mechanical displacements and strains can be mapped with micron-scale resolution in engineered tissue cultures as groups of cells begin to proliferate and attach within a three-dimensional collagen matrix. We have also demonstrated this method in the more complex developing tissues of a standard developmental biology animal model (*Xenopus laevis*). After applying uniform external static compressions, displacements were quantified by utilizing a custom cross-correlation algorithm on the pre- and postcompression images, which were acquired using OCT. The images were taken after specific periods of time to observe the relative strain differences as groups of cells began to proliferate and become organized. Displacement and strain maps were computed and shown, along with corresponding histological images to validate our findings.

According to our results, we infer that the cells seeded into our matrix underwent a short period of recovery from the environmental shock of seeding, before beginning to proliferate and form attachments. However, as incubation time increases, cell proliferation and cell-cell and cell-matrix adhesions increase. As a result, a more mechanically robust, stiffer microstructure forms within the engineered tissue, which increases the ability of the engineered tissue to sustain external compression. A decrease in strain and displacement within the cell-seeded region on days 7 and 10 compared with the cell-free region demonstrates this trend. Although the fitted line in Figure 3 assumes a linear relationship to show the general trend, a nonlinear curve is most likely since cells proliferate in a nonlinear fashion before reaching a steady-state condition.

While our current technology for engineering tissues has advanced in recent years, our understanding of the complex biomechanical properties in developing engineered tissues or biological specimens has been limited. OCE has the potential to provide both a qualitative and quantitative means for characterizing the biomechanical properties at the micron scale within highly scattering tissues in real-time and longitudinally in single tissue cultures or biological specimens throughout development.

In future studies, improvements in OCT instrumentation for OCE can be incorporated to provide even more accurate assessments of biomechanical properties within engineered and developing tissues. If imaging with higher transverse resolution is desired, focus-tracking could be implemented, which raster-scans the small focal region and coherence gate throughout the imaging plane, rather than performing sequential axial (depth) scans by translating the reference arm retro-reflector. Varying types and sizes of scattering objects may be used in the engineered tissue in place of the polystyrene microspheres used in this study. These scattering objects could play a more functional role, such as a biodegradable or encapsulating microsphere containing cell growth factors, nutrients, or specific biochemical modulators. Degradable microspheres would also mitigate the increase of scattering at later growth stages as the cells begin proliferating and depositing extracellular matrix. By implementing higher speed time- or spectral-domain OCT techniques, acquisition time can be significantly reduced to allow real-time observation of dynamic compression, including viscoelastic properties, which can deviate significantly from static compression, especially for *in vivo* measurements where strain at each point depends on the elasticity distribution in the adjacent tissues as well as different applied pre-loads. Three-dimensional OCT data volumes can be acquired and used to track individual displacements in three dimensions, eliminating possible loss of particle displacements from two-dimensional images. Finally, one may consider developmental biology animal models as essentially complex engineered tissues. By improving our understanding and characterization of the biomechanical properties within these animal models, OCE data may provide new insight into the relationships between cell and tissue biomechanics and tissue development and function.

The combination of OCT and elastography is likely to provide researchers with an opportunity to link microstructural data with biomechanical and functional information. Moreover, OCE is likely to have a broad impact in a wide range of applications in the field of tissue engineering. By quantifying biomechanical properties within engineered tissues and animal models using OCE and by relating specific regions to unique functions, one can begin to investigate how similar biomechanical properties in engineered tissues can be induced by modifying different mechanical stimuli during culture, opening the possibility of using mechanical stimuli to shape engineered tissue structure and function. Ultimately, the new data generated using OCE may improve our ability to de-

velop a more biocompatible and biomimetic engineered tissue.

REFERENCES

1. Shiraishi, Y., Kobayashi, M., Yasui, M., Ozaki, N., and Sugiura, Y. Innervation and functional characteristics of connective tissues, especially elastic fibers, in human fetal thoracic intervertebral articular capsule and its surroundings. Anat. Embryol. **206,** 437, 2003.

2. Springer, A.D., and Hendrickson, A.E. Development of the primate area of high acuity. Use of finite element analysis models to identify mechanical variables affecting pit formation. Vis. Neurosci. **21,** 53, 2004.

3. Yang, C.M., Chien, C.S., Yao, C.C., Hsiao, L.D., Huang, Y.C., and Wu, C.B. Mechanical strain induces collagenase-3 (MMP-13) expression in MC3T3-E1 osteoblastic cells. J. Biol. Chem. **279,** 22158, 2004.

4. Bastos, A.L., Silva, E.A., Silva Costa, W., and Sampaio, F.J. The concentration of elastic fibres in the male urethra during human fetal development. Br. J. Urol. **94,** 620, 2004.

5. Birnholz, J.C., and Farrell, E.E. Fetal lung development: compressibility as a measure of maturity. Radiology **157,** 495, 1985.

6. Hunter, C.J., Imler, S.M., Malaviya, P., Nerem, R.M., and Levenston, M.E. Mechanical compression alters gene expression and extracellular matrix synthesis by chondrocytes cultured in collage I gels. Biomaterials **23,** 1249, 2002.

7. Costa, K.D. Single-cell elastography: Probing for disease with the atomic force microscope. Dis. Markers **19,** 139, 2004.

8. Plewes, D.B., Bishop, J., Samani, A., and Sciarretta, J. Visualization and quantification of breast cancer biomechanical properties with magnetic resonance elastography. Phys. Med. Biol. **45,** 1591, 2000.

9. Wu, T., Felmlee, J.P., Greenleaf, J.F., Riederer, S.J., and Ehman, R.L. Assessment of thermal tissue ablation with MR elastography. Mag. Reson. Med. **45,** 80, 2001.

10. Bercoff, J., Chaffai, S., Tanter, M., Sandrin, L., Catheline, S., Fink, M., Gennisson, J.L., and Meunier, M. *In vivo* breast tumor detection using transient elastography. Ultrasound Med. Biol. **29,** 1387, 2003.

11. Han, L., Noble, J.A., and Burcher, M. A novel ultrasound indentation system for measuring biomechanical properties of *in vivo* soft tissue. Ultrasound Med. Biol. **29,** 813, 2003.

12. Bilgen, M., Srinivasan, S., Lachman, L.B., and Ophir, J. Elastography imaging of small animal oncology models: a feasibility study. Ultrasound Med. Biol. **29,** 1291, 2003.

13. Liu, H.T., Sun, L.Z., Wang, G., and Vannier, M.W. Analytic modeling of breast elastography. Med. Phys. **30,** 2340, 2003.

14. Timoshenko, S. P., and Goodier, J.N. Theory of Elasticity. New York: McGraw-Hill, 1970, pp. 403–409.

15. Ophir, J., Kallel, F., Varghese, T., Konofagou, E., Alam, S.K., Krouskop, T., Garra, B., and Righetti, R. Elastography. Opt. Acous. Imaging Biol. Media **2,** 1193, 2001.

16. Parker, K.J., Gao, L., Lerner, R.M., and Levinson, S. F. Techniques for elastic imaging: a review. IEEE Eng. Med. Biol. Mag. **15,** 52, 1996.

17. Karcher, H., Lammerding, J., Huang, H., Lee, R.T., Kamm, R.D., and Kaazempur-Mofrad, M.R. A three-dimensional viscoelastic model for cell deformation with experimental verification. Biophys. J. **85,** 3336, 2003.

18. Khatyr, F., Imberdis, C., Vescovo, P., Varchon, D., and Lagarde, J.M. Model of the visoelastic behaviour of skin *in vivo* and study of anisotropy. Skin Res. Technol. **10,** 96, 2004.

19. Ko, F.K., and Jovicic, J. Modeling of mechanical properties and structural design of spider web. Biomacromolecules **5,** 780, 2004.

20. Lorenzen, J., Sinkus, R., and Adam G. Elastography: quantitative imaging modality of the elastic tissue properties. Rofo **175,** 623, 2003.

21. Sinkus, R., Tanter, M., Catheline, S., Lorenzen, J., Kuhl, C., Sondermann, E., and Fink, G. Imaging anisotropic and viscous properties of breast tissue by magnetic resonance elastography. Magn. Reson. Med. **53,** 372, 2005.

22. Suga, M., Matsuda, T., Minato, K., Oshiro, O., Chihara, K., Okamoto, J., Takizawa, O., Komori, M., and Takahashi, T. Measurement of *in-vivo* local shear modulus by combining multiple phase offsets MR elastography. Medinfo **10,** 933, 2001.

23. Wilson, L.S., Robinson, D.E., and Dadd, M.J. Elastography: The movement begins. Phys. Med. Biol. **45,** 1409, 2000.

24. Righetti, R., Ophir, J., and Ktonas, P. Axial resolution in elastography. Ultrasound Med. Biol. **28,** 101, 2002.

25. Huang, D., Swanson, E. A., Lin, C. P., Schuman, J. S., Stinson, W. G., Chang, W., Hee, M. R., Flotte, T., Gregory, K., and Puliafito, C. A., and Fujimoto, J.G. Optical coherence tomography. Science **254,** 1178, 1991.

26. Bouma, B.E., and Tearney, G.J. Handbook of Optical Coherence Tomography. New York: Marcel Dekker, 2001.

27. Takada, K., Yokohama, I., Chida, K., and Noda, J. New measurement system for fault location in optical waveguide devices based on an interferometric technique. Appl. Opt. **26,** 1603, 1987.

28. Gilgen, H.H., Novak, R.P., Salathe, R.P., Hodel, W., and Beaud, P. Submillimeter optical reflectometry. J. Lightwave Tech. **7,** 1225, 1989.

29. Youngquist, R.C., Carr, S., and Davies, D. Optical coherence-domain reflectometry: a new optical evaluation technique. Opt. Lett. **12,** 158, 1987.

30. Swanson, E.A., Huang, D., Hee, M.R., Fujimoto, J.G., Lin, C.P., and Puliafito, C.A. High-speed optical coherence domain reflectometry. Opt. Lett. **17,** 151, 1992.

31. Schuman, J.S., Hee, M.R., Puliafito, C.A., Wong, C., Pedutkloizman, T., Lin, C.P., Hertzmark, E., Izatt, J.A., Swanson, E.A., and Fujimoto, J.G. Quantification of nerve-fiber layer thickness in normal and glaucomatous eyes using optical coherence tomography. Arch. Ophthalmol. **113,** 586, 1995.

32. Brezinski, M.E., Tearney, G.J., Bouma, B.E., Izatt, J.A., Hee, M.R., Swanson, E.A., Southern, J.M., and Fujimoto, J.G. Optical coherence tomography for optical biopsy: properties and demonstration of vascular pathology. Circulation **93,** 1206, 1996.

33. Brezinski, M.E., Tearney, G.J., Weissman, N.J., Boppart, S.A., Bouma, B.E., Hee, M.R., Weyman, A.E., Swanson, E.A., Southern, J.F., and Fujimoto, J.G. Assessing atherosclerotic plaque morphology: comparison of optical coherence tomography and high frequency intravascular ultrasound. Heart **77,** 397, 1997.

34. Tearney, G.J., Brezinski, M.E., Southern, J.F., Bouma, B.E., Boppart, S.A., and Fujimoto, J.G. Optical biopsy in human gastrointestinal tissue using optical coherence tomography. Am. J. Gastroenterol. **92,** 1800, 1997.

35. Tearney, G.J., Brezinski, M.E., Southern, J.F., Bouma, B.E., Boppart, S.A., and Fujimoto, J.G. Optical biopsy in human urologic tissue using optical coherence tomography. J. Urol. **157,** 1915, 1997.

36. Boppart, S.A., Brezinski, M.E., Bouma, B.E., Tearney, G.J., and Fujimoto, J.G. Investigation of developing embryonic morphology using optical coherence tomography. Dev Biol. **177,** 54, 1996.

37. Boppart, S.A., Bouma, B.E., Brezinski, M.E., Tearney, G.J., and Fujimoto, J.G. Imaging developing neural morphology using optical coherence tomography. J. Neurosci. Methods **70,** 65, 1996.

38. Boppart, S.A., Tearney, G.J., Bouma, B.E., Southern, J.F., Brezinski, M.E., and Fujimoto, J.G. Noninvasive assessment of the developing *Xenopus* cardiovascular system using optical coherence tomography. Proc. Natl. Acad. Sci. USA **94,** 4256, 1997.

39. Yelbuz, T.M., Choma, M.A., Thrane, L., Kirby, M.L., and Izatt, J.A. Optical coherence tomography: a new high-resolution imaging technology to study cardiac development in chick embryos. Circulation **106,** 2771, 2002.

40. Xu, X., Wang, R.K., and El Haj, A. Investigation of changes in optical attenuation of bone and neuronal cells in organ culture or three-dimensional constructs *in vitro* with optical coherence tomography: relevance to cytochrome oxidase monitoring. Eur. Biophys. J. **32,** 355, 2003.

41. Mason, C., Markusen, J.F., Town, M.A., Dunnill, P., and Wang, R.K. The potential of optical coherence tomography in the engineering of living tissue. Phys. Med. Biol. **49,** 1097, 2004.

42. Schmitt, J.M. OCT elastography: imaging microscopic deformation and strain of tissue. Opt. Express **3,** 6, 1998.

43. Rogowska, J., Patel, N.A., Fujimoto, J.G., and Brezinski, M.E. Optical coherence tomographic elastography technique for measuring deformation and strain of atherosclerotic tissues. Heart **9,** 556, 2004.

44. Hajinikolaou, L., Kotidis, K., and Galinanes, M. Relationship between reduced elasticity of extracardiac vessels and left main stem coronary artery disease. Eur. Heart J. **25,** 508, 2004.

45. Chan, R.C., Chau, A.H., Karl, W.C., Nadkarni, S., Khalil, A.S., Iftimia, N., Shishkov, M., Tearney, G.J., Kaazempur-Mofrad, M.R., and Bouma, B.E. OCT-based arterial elastography: robust estimation exploiting tissue biomechanics. Opt. Express **12,** 4558, 2004.

46. Marks, D.L., Oldenburg, A.L., Reynolds, J.J., and Boppart, S.A. Study of an ultrahigh-numerical-aperture fiber continuum generation source for optical coherence tomography. Opt. Lett. **27,** 2010, 2002.

Address reprint requests to:
Stephen A. Boppart, M.D., Ph.D.
Beckman Institute
University of Illinois at Urbana-Champaign
405 N. Mathews Avenue
Urbana, IL 61801

E-mail: boppart@uiuc.edu